Concrete meso-scale model with full set of 3D failure modes with random distribution of aggregate and cement phase. Part I: Formulation and numerical implementation

Emir Karavelić, Mijo Nikolić, Adnan Ibrahimbegovic, Azra Kurtović

Available online at www.sciencedirect.com
ScienceDirect
Comput. Methods Appl. Mech. Engrg. 344 (2019) 1051–1072
Computer methods in applied mechanics and engineering
www.elsevier.com/locate/cma

Concrete meso-scale model with full set of 3D failure modes with random distribution of aggregate and cement phase. Part I: Formulation and numerical implementation

Emir Karavelić[a,b], Mijo Nikolić[c], Adnan Ibrahimbegovic[a,*], Azra Kurtović[b]

[a] *Université de Technologie de Compiègne/Sorbonne Universités, Laboratoire Roberval de Mécanique, Centre de Recherche Royallieu, 60200 Compiègne, France*
[b] *University of Sarajevo, Faculty of Civil Engineering, 71000 Sarajevo, Bosnia and Herzegovina*
[c] *University of Split, Faculty of Civil Engineering, Architecture and Geodesy, 21000 Split, Croatia*

Received 16 May 2017; received in revised form 6 September 2017; accepted 8 September 2017
Available online 2 October 2017

Abstract

Prediction of failure mechanisms in concrete is a fairly complex task due to heterogeneous concrete microstructure, localization process triggered by cracks, multiple crack interactions during their growth and coalescence, and different dissipative mechanisms in a fracture process zone prior to localized failure and in a localization zone during the failure. None of the currently used phenomenological models can represent the full set of 3D failure modes. This work presents an attempt to solve this with the 3D meso-scale model based on discrete lattice approach. In particular we show that we can capture such complexities at the meso-scale, which is able to represent microcracks in fracture process zone along with the localized failure represented in terms of embedded strong discontinuity and accompanied with softening constitutive law. The model can also successfully simulate salient features of concrete response, such as order of magnitude of reduction in strength in uniaxial tension versus compression, strength increase in biaxial loading or hydrostatic tension. Moreover, macro-scale representation of failure surfaces obtained with presented model for different loading programs confirms the need for failure concrete criterion of multi-surface kind. Part I of this work presents the proposed meso-scale based on extensive number of numerical simulations with multiple realizations of different concrete specimens, along as the optimal deterministic fit for several common concrete failure models. The ultimate interest of the work is to provide detailed data set for different failure modes which can be used for identification of probability distribution of material parameters for different criteria. Such task is carried in Part II of this work.

Keywords: Concrete 3D failure mechanisms; Discrete lattice model; Localized failure; Embedded discontinuity; Parameter identification

1. Introduction

The key assumption explored in this work pertains to the role of material heterogeneity in a study of the mechanical behavior and failure modes in concrete. When a concrete specimen under extreme loading condition enters in the stage

* Corresponding author.
E-mail address: adnan.ibrahimbegovic@utc.fr (A. Ibrahimbegovic).

http://dx.doi.org/10.1016/j.cma.2017.09.013
0045-7825/

where localized cracks and displacement discontinuities appear, the most appropriate model changes from continuous into discrete one. Crack propagation and final crack patterns in concrete are mostly based on accumulated microcracks of various kinds of initial flaws, defects in aggregate structures, voids or pores inside concrete caused during fabrication. These processes of accumulation of microcracks lead to a complete set of 3D failure mechanisms, usually governed by multiple crack interactions, growth and coalescence producing the brittle type failure characteristic for concrete. In order to provide a reliable predictive model for failure of such heterogeneous materials, we build the model at meso-scale. The approach we focus upon in this paper relies on spatial beam models [1], as a class of discrete lattice models [2]. For each random distribution realization of aggregate geometry is built using Delaunay triangulation. Such approach has an advantage of representing the multi-phase structure of concrete, namely cement paste and aggregates, and can provide the localized failure mechanisms with respect to heterogeneities. Here, the Delaunay edges in triangulation can be considered as lattice elements representing cohesive links between the Voronoi cells, each filled-in with a single phase of heterogeneous material (Fig. 1(a)). Lattice elements are simulated with 3D Timoshenko beams which allow to represent the complete set of 3D failure modes. The Voronoi cells can guarantee the exact representation of linear elastic isotropic response, considering the concrete statistically as an isotropic material. The geometrical properties of the beams can be extracted from the common area between the two neighboring Voronoi cells (Fig. 1(b)).

Another advantage of the chosen discrete model is the ability to account all failure modes, I, II and III. The only remaining difficulty in the failure analysis is to provide mesh-independent representation of the post-peak softening behavior [3]. The main idea in large number of lattice meso-scale models is that lattice elements progressively fail (leading to softening behavior in failed elements) which eventually results in total macroscopic failure. However, there is still an ongoing problem of how to represent correctly the post peak softening behavior, which is normally dependent on the mesh. This pertains to released fracture energy (i.e. area below the softening curve) which is not unique for different mesh sizes. Avoiding this fact can lead not only to wrong global fracture energy and wrong post peak response, but it can also underestimate the global fracture limits. Many lattice element models use sequentially linear algorithms to avoid negative stiffness terms and deals with mesh-dependence by performing additional regularization procedures with scaling initial strength and ultimate strain on the local element level to obtain correct fracture energy on a global level [4]. Some other models use incremental (sometimes also iterative) schemes in time, but the problem of fracture energy depending on mesh still remains, like in standard finite elements. One of the ways to provide mesh independent response is by using embedded strong discontinuity approach [5,6], which is generalized to include the fracture process zone [7,8]. The main reason for this mesh independence is that discontinuity, or displacement jump, always remains localized inside the element. This approach can be interpreted as a localization limiter that enhances the classical continuum mechanics theoretical formulation by admitting discontinuities in the displacement field. The numerical implementation of the discontinuity requires a modification of the standard finite element procedure, which is similar to the method of incompatible modes [9].

Embedded discontinuity formulation is developed here to enhance the 3D Timoshenko beam lattice elements to provide all three failure modes characteristic for concrete. The model is adopted from our previous works dealing with failure of rocks [10–12].

The adaptation concerns the microstructure representation being aggregate in agreement with the granulometric curve. In other words, we recognize that the concrete is highly a heterogeneous composite material. One can distinguish between the two phases of the material at the observational meso-scale. The meso-scale can capture fundamental aspects of material heterogeneity without being computationally too expensive [13]. Various models of concrete failure can be found in the literature [13–22], none of them are comparable to the present model that provides all failure modes I, II and III in terms of embedded discontinuities in Timoshenko lattice beam elements. By using only mode I at meso-scale we can successfully represent simple tension test, or even be able to deal with 3 point bending test when bending failure (not shear) remains the dominant failure mode. However, the failure modes of concrete composites are more complex, in anything else from simple tension. The model for concrete failure restricted to truss bars and embedded discontinuities providing only mode I failure could get only 1:5 overall ratio between uniaxial tension and compression [23,24]. The model concerning mode I at the meso-scale proposed by [25] is positioning the cohesive links in the direction of stress principal axes, which automatically eliminates the contribution of shear. Lattice elements in this case are perfectly brittle upon reaching failure criterion, when they are physically removed from mesh. The algorithm for the solution of equations fitting into this framework is based on sequentially linear analysis, which does not have the same stringent equilibrium enforcing properties, as the method proposed in this paper, where lattice

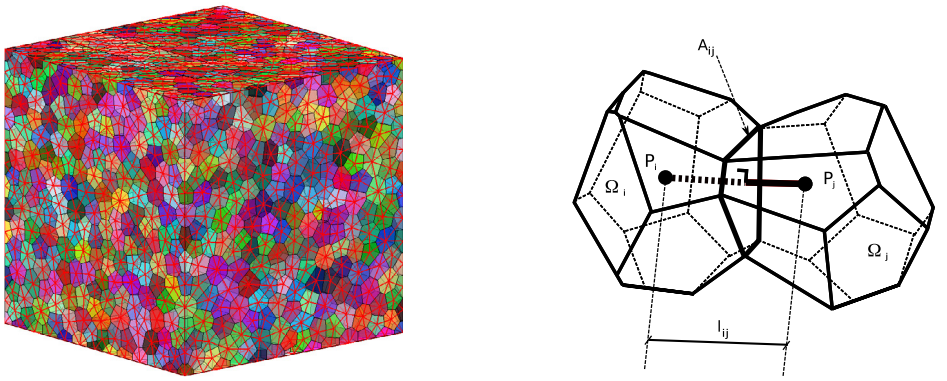

Fig. 1. (a) Structure of discrete lattice model with Voronoi cells as units of heterogeneous material and cohesive links between them; (b) two neighboring Voronoi cells.

elements are not removed from mesh after reaching failure criterion, but they go into softening regime in agreement with defined fracture energy for modes I, II and III. Shear failure mechanisms contribute here mostly through the presence of aggregate in concrete composite, which makes the crack deviate from shortest (orthogonal) path and introduces the contribution of modes II and III. Here, the failure criteria include modes II and III, together with Mohr–Coulomb law on local element level for shear failure under compression. Macroscopic mechanical response depends strongly on each phase properties, both for cement paste and aggregates, as well as on their spatial distribution. Spatial distribution of each phase is spread here with random process with the Poisson distribution of the aggregates (phase I) subsequently filling the voids between them with cement paste (phase II). The distribution of aggregate size is taken in agreement with one of the two well-known aggregates grading curves in the concrete mixture [26]. The choice is made that all particles with size less than 2.0 mm be included in cement matrix volume, thus forming cement mortar. By using this way of distribution we are able to obtain the realistic values of phase volume fraction. The Gaussian distribution of the material properties heterogeneity in each phase (aggregate and cement paste) is taken into account with standard deviation restricted to $\pm\ 2\sigma$. Such distribution of material properties takes into account the weakening of concrete through Interface Transition Zone (ITZ), whose properties are considered heterogeneous and represent weak spots in concrete decided by random process through the distribution of material properties for cement paste, from where the cracks are then triggered.

Various types of phenomenological constitutive models are widely used in structural scale computations for prediction of behavior in static or dynamic cases [27,28]. In adopting to the case of a complex loading program, these models require choice of the elaborate and equally complex criterion. Because of their macroscopic point of view, these models encounter insurmountable difficulties in describing correctly the fine scale physical mechanisms, such as fracture or damage. The proposed meso-scale model can improve this and provide different failure mechanisms leading to macro-scale representation typically given in terms of multi-surface failure criterion for concrete. In order to identify the most appropriate failure criterion, we carry out large number of numerical tests at fine scale with different loading programs. In particular, we consider the uniaxial tension and compression, biaxial tests with strength increase and hydrostatic tension. We thus obtain different values for compression and tension strength as a function of aggregate volume fraction.

The outline of the paper is as follows: In Section 2 we describe the meso-scale model, with the cohesive links in terms of Timoshenko beam elements. In Section 3, we present the results of numerical simulations with the ultimate goal of computing corresponding macro-scale failure surface obtained with meso-scale model computations. Section 4 summarizes the conclusion regarding all the main findings and suggests the perspective studies.

2. Meso-scale model for concrete failure

In this section we give a description of the meso-scale model of concrete constitutive behavior as a two phase material. First, the 3D Delaunay triangulation [29] is performed in certain volume, representing the specimen. Second, the Voronoi diagram is extracted from Delaunay triangulation resulting with Voronoi cells that occupy smaller part

of the volume. The size of the Voronoi cells should correspond to the representative size of heterogeneities, and thus form the grains in the material (Fig. 1). Voronoi cells should be initially kept together, like grains, with cohesive forces which are represented by the beam lattice network extracted from Delaunay triangulation edges [30].

Phase I, chosen as the aggregate, is spatially spread across specimen by using the Poisson distribution seeking to achieve the corresponding grading curves for aggregate [26]. Two well-known grading curves, EMPA and Fuller (Fig. 2), are defined with relations

$$\begin{aligned} p(d_{Fuller}) &= 100\sqrt{\frac{d}{d_{max}}} \\ p(d_{EMPA}) &= 50\left(\frac{d}{d_{max}} + \sqrt{\frac{d}{d_{max}}}\right) \end{aligned} \tag{1}$$

where $p(d_F)$ and $p(d_E)$ are the cumulative percent passing through a sieve with diameter d, white d_{max} as the diameter of the coarsest aggregate. We consider here the distribution of aggregate as an arithmetic mean of these two grading curves where all particles smaller than 2.00 mm are included in cement matrix volume forming cement mortar. The second, separate study of this phase is not necessary since formation of cement or mortar layer can be determined based on the distribution of the aggregates. According to the defined grading curve we use in further study, the aggregate with maximal diameter of 8 mm, 16 mm and 32 mm obtaining, respectively, 30%, 50% and 60% volume fraction for phase I.

Each phase material properties are assigned to the corresponding beam elements which fall inside the particular phase. The geometric properties of beams are extracted from the Voronoi diagram. Namely, the common area of the two neighboring Voronoi cells (Fig. 1(b)) is approximated by circular cross section and is used to compute the single beam diameter, from which the beam cross-section parameters are obtained [12]. This leads to the lattice of thick beams which can be represented by Timoshenko beam elements accounting for shear deformation. One can write the standard kinematics for 3D Timoshenko beam element with length l_e

$$\begin{aligned} \epsilon(x) &= \frac{du(x)}{dx} \\ \gamma_y(x) &= \frac{dv(x)}{dx} - \theta(x) \\ \gamma_z(x) &= \frac{dw(x)}{dx} + \psi(x) \\ \kappa_x(x) &= \frac{d\varphi(x)}{dx} \\ \kappa_y(x) &= \frac{d\psi(x)}{dx} \\ \kappa_z(x) &= \frac{d\theta(x)}{dx}. \end{aligned} \tag{2}$$

By using the matrix notation, the Timoshenko beam strains are placed in a vector that can be written as $\boldsymbol{\epsilon} = \begin{bmatrix} \epsilon & \gamma_y & \gamma_z & \kappa_x & \kappa_y & \kappa_z \end{bmatrix}^T$. Vector $\mathbf{u} = \begin{bmatrix} u & v & w & \varphi & \psi & \theta \end{bmatrix}^T$ represents the beam axis displacements and cross-section notations as shown in Fig. 3.

In order to represent the three failure modes in concrete, we consider the discontinuities in the generalized displacement field of the 3D Timoshenko beam. Such enhancements of 3D Timoshenko beam can provide mode I as axial failure mode and modes II and III as shear failure modes between the Voronoi cells (Fig. 4). To that end, the standard beam displacements are enhanced with the Heaviside function and decomposed into regular and singular parts in the following way:

$$\mathbf{u}(x) = \overline{\mathbf{u}}(x) + \boldsymbol{\alpha} H_{x_c} = \begin{bmatrix} \overline{u}(x) \\ \overline{v}(x) \\ \overline{w}(x) \\ \overline{\varphi}(x) \\ \overline{\psi}(x) \\ \overline{\theta}(x) \end{bmatrix} + \begin{bmatrix} \alpha_u \\ \alpha_v \\ \alpha_w \\ 0 \\ 0 \\ 0 \end{bmatrix} H_{x_c}. \tag{3}$$

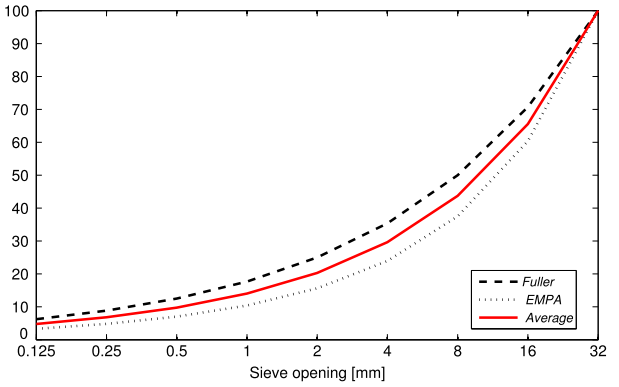

Fig. 2. Grading curves.

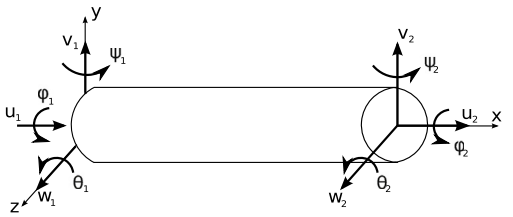

Fig. 3. 3D Timoshenko beam displacements.

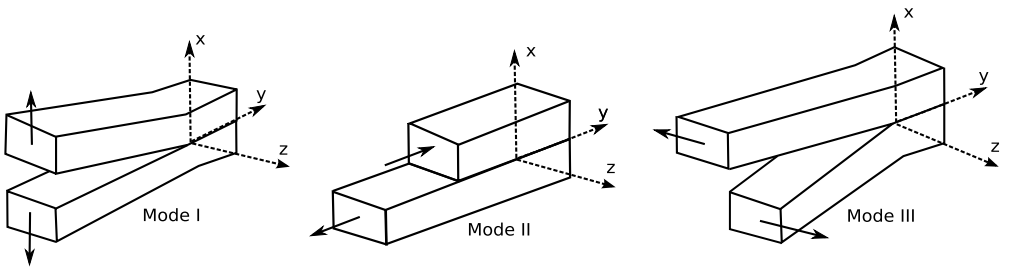

Fig. 4. Three failure modes in concrete.

Here, H_{x_c} is the Heaviside function defined by $H_{x_c}(x) = 0$ for $x \leq x_c$ and $H_{x_c}(x) = 1$ for $x > x_c$ and $\boldsymbol{\alpha} = [\alpha_u \quad \alpha_v \quad \alpha_w \quad 0 \quad 0 \quad 0]^T$ represents the vector of displacement jumps at the point of discontinuity, which is positioned exactly in the middle of the beam. This is also the point where two neighboring Voronoi cells share the same side.

One can rewrite Eq. (3) by adding and subtracting a regular differentiable function ϕ from the Heaviside function, which will produce the following form of displacement field:

$$\mathbf{u}(x) = \underbrace{\overline{\mathbf{u}}(x) + \boldsymbol{\alpha}\phi(x)}_{\text{regular part}} + \underbrace{\boldsymbol{\alpha}(H_{x_c} - \phi(x))}_{\text{localized part}}. \tag{4}$$

In the context of finite elements, the regular part of displacement field is interpolated with standard shape functions. On the other side, localized part requires additional treatment which can be handled within the framework of incompatible modes [9], with element modification for localized discontinuity. The enhanced strain field is obtained through the Dirac delta δ_{x_c} resulting from the derivative of the Heaviside function multiplying a discontinuous

displacement field from above.

$$\boldsymbol{\epsilon}(x) = \tilde{\boldsymbol{\epsilon}}(x) + G\boldsymbol{\alpha} + \boldsymbol{\alpha}\delta_{x_c} \tag{5}$$

where $\tilde{\boldsymbol{\epsilon}}$ represents the regular part of the strain field obtained from the regular part of the displacement field in Eq. (4). Operator G is defined as $L(-\phi(x))$, where L is the strain–displacement operator.

The finite element interpolation of the total displacement field from Eq. (3) can be written as

$$\mathbf{u}(x) = N_1(x)\overline{\mathbf{u}}_1 + N_2(x)\overline{\mathbf{u}}_2 + \boldsymbol{\alpha} H_{x_c} \tag{6}$$

where the interpolation of the regular part of Timoshenko beam displacements can be performed with linear polynomials as shape functions, namely $N_1(x) = 1 - \frac{x}{l_e}$, $N_2(x) = \frac{x}{l_e}$. Vectors $\overline{\mathbf{u}}_1$ and $\overline{\mathbf{u}}_2$ are the nodal vectors of regular displacement part from (3) related to element nodes 1 and 2, respectively. Total displacements for nodes 1 and 2 can be written in terms of displacements of the regular part as

$$\begin{aligned} \mathbf{u}(x_1) &= \mathbf{u}_1 = \overline{\mathbf{u}}_1 \\ \mathbf{u}(x_2) &= \mathbf{u}_2 = \overline{\mathbf{u}}_2 + \boldsymbol{\alpha} \end{aligned} \tag{7}$$

and expression (6) can be rewritten with $\overline{\mathbf{u}}_2 = \mathbf{u}_2 - \boldsymbol{\alpha}$ in terms of total displacements as

$$\mathbf{u}(x) = N_1(x)\mathbf{u}_1 + N_2(x)\mathbf{u}_2 + \boldsymbol{\alpha} \underbrace{\left(H_{x_c} - N_2(x)\right)}_{M(x)}. \tag{8}$$

One can note that function $\phi(x)$ from (4) can be taken as $\phi(x) = N_2(x)$ for the chosen linear interpolation. Second part in (8), related to incompatible mode, can be denoted as interpolation function $M(x)$ for the discontinuity

$$M(x) = \begin{cases} -\dfrac{x}{l_e}; x \in [0, x_c\rangle \\ 1 - \dfrac{x}{l_e}; x \in \langle x_c, l_e]. \end{cases} \tag{9}$$

The interpolation of total displacement field from (8) can thus be re-written in the matrix form as

$$\mathbf{u} = \mathbf{N}\mathbf{u}_a + \mathbf{M}\boldsymbol{\alpha} \tag{10}$$

with $\mathbf{N}$ being 6×12 element shape function matrix containing functions $N_1(x)$ and $N_2(x)$, $\mathbf{u}_a = \begin{bmatrix}\mathbf{u}_1 & \mathbf{u}_2\end{bmatrix}^T$ and $\mathbf{M}$ is the 6×6 matrix of discontinuity interpolation functions M positioned at the diagonal first three entries related to translational degrees of freedom.

In order to obtain the interpolated enhanced strain field, one needs to consider the derivatives of shape functions $B_1(x) = -\frac{1}{l_e}$, $B_2(x) = \frac{1}{l_e}$ and the derivative of discontinuity interpolation function, leading to

$$G(x) = \overline{G}(x) + \delta_{x_c}, \quad \overline{G}(x) = -\frac{1}{l_e}. \tag{11}$$

The function G is split into regular part $\overline{G}$ and singular part in terms of δ_{x_c}. With preferred choice of ϕ, the expression above reduces to $\overline{G}(x) = -B_2(x)$. The interpolated enhanced strain field can finally be obtained with

$$\boldsymbol{\epsilon} = \mathbf{B}\mathbf{u}_a + \overline{\mathbf{G}}\boldsymbol{\alpha} + \boldsymbol{\alpha}\delta_{x_c} \tag{12}$$

where $\mathbf{B}$ is the 6×12 beam strain–displacement matrix corresponding to Eq. (2) and $\overline{\mathbf{G}}$ is the 6×6 matrix of derivatives of discontinuity interpolation function $\overline{G}$ at the entries related to translational degrees of freedom.

The same kind of interpolations for virtual strain field is used to construct the weak form of equilibrium equations:

$$\delta\boldsymbol{\epsilon} = \mathbf{B}\delta\mathbf{u}_a + \overline{\mathbf{G}}_v\delta\boldsymbol{\alpha} + \delta\boldsymbol{\alpha}\delta_{x_c} \tag{13}$$

where $\delta\mathbf{u}_a$ and $\delta\boldsymbol{\alpha}$ denote the total virtual displacement field and virtual displacement jump, respectively. Enforcement of orthogonality between the enhanced strain and constant stress is needed within the element by fulfilling the patch test condition [9]

$$\mathbf{G}_v = \mathbf{G} - \frac{1}{l_e}\int_0^{l_e} \mathbf{G}dx. \tag{14}$$

For this element, where reduced one Gauss point integration is used, it holds that $\mathbf{G}_v = \mathbf{G}$.

The virtual work equation can be written at element level

$$G^{int,(e)} - G^{ext,(e)} = 0 \tag{15}$$

where $G^{int,(e)} = \int_0^{l_e} (\delta\boldsymbol{\epsilon})^T \boldsymbol{\sigma} dx$. By replacing the virtual strain field from (13) into virtual work equation, we end up with a set of two equations:

$$\begin{aligned} &\int_0^{l_e} (\delta \mathbf{u}_a) \mathbf{B}^T \boldsymbol{\sigma} dx = G^{ext} \\ &\int_0^{l_e} (\delta\boldsymbol{\alpha})(\overline{\mathbf{G}} + \boldsymbol{\delta}_{x_c})^T \boldsymbol{\sigma} dx = 0. \end{aligned} \tag{16}$$

The standard internal force vector $\mathbf{f}^{int,(e)}$ is obtained from the standard part of internal virtual work, while the enhanced part produces the element residual $\mathbf{h}^{(e)}$ at discontinuity. By using the standard finite element assembly procedure, we get

$$\begin{aligned} &A_{e=1}^{n_{el}} \left(\mathbf{f}^{int,(e)} - \mathbf{f}^{ext} \right) = 0 \\ &\mathbf{h}^{(e)} = \int_0^{l_e} \overline{\mathbf{G}}^T \boldsymbol{\sigma} dx + \mathbf{t}, \quad \forall e \in [1, n_{el}] \end{aligned} \tag{17}$$

where $f^{int,(e)} = \int_0^{l_e} \mathbf{B}^T \boldsymbol{\sigma} dx$. The condition $\mathbf{h}^{(e)} = 0$ needs to be enforced for each element where discontinuity is activated, which leads to definition of the traction vector at discontinuity

$$\mathbf{t} = -\int_0^{l_e} \overline{\mathbf{G}} \boldsymbol{\sigma} dx. \tag{18}$$

Note that assembly operator in the first equation in (17) considers all elements, while the second equation remains limited to a particular element due to the character of the interpolation function for discontinuity which takes zero values at the element boundary.

In order to solve the nonlinear problem in (17), the consistent linearization of both equations has to be performed. The standard Newton incremental–iterative procedure is used to provide new iterative values of nodal displacements.

$$\begin{aligned} &A_{e=1}^{n_{el}} \left[\mathbf{K}_{n+1}^{e,(i)} \Delta \mathbf{u}_{n+1}^{(i)} + \mathbf{F}_{n+1}^{e,(i)} \Delta \boldsymbol{\alpha}_{n+1}^{(i)} \right] = A_{e=1}^{n_{el}} \left[\mathbf{f}_{n+1}^{ext,e} - \mathbf{f}_{n+1}^{int,e,(i)} \right] \\ &\mathbf{h}_{n+1}^{e,(i)} + \left(\mathbf{F}_{v,n+1}^{e,(i)} + \mathbf{K}_{d,n+1}^{(i)} \right) \Delta \mathbf{u}_{n+1}^{(i)} + \left(\mathbf{H}_{n+1}^{e,(i)} + \mathbf{K}_{\alpha,n+1}^{(i)} \right) \Delta \boldsymbol{\alpha}_{n+1}^{(i)} = 0 \end{aligned} \tag{19}$$

where the explicit form of matrices are

$$\begin{aligned} &\mathbf{K}_{n+1}^{e,(i)} = \int_0^{l_e} \mathbf{B}^T \mathbf{C}_{n+1}^{(i)} \mathbf{B} dx, \quad \mathbf{F}_{n+1}^{e,(i)} = \int_0^{l_e} \mathbf{B}^T \mathbf{C}_{n+1}^{(i)} \overline{\mathbf{G}} dx \\ &\mathbf{F}_{v,n+1}^{e,(i)} = \int_0^{l_e} \overline{\mathbf{G}}^T \mathbf{C}_{n+1}^{(i)} \mathbf{B} dx, \quad \mathbf{H}_{n+1}^{e,(i)} = \int_0^{l_e} \overline{\mathbf{G}}^T \mathbf{C}_{n+1}^{(i)} \overline{\mathbf{G}} dx \end{aligned} \tag{20}$$

and $\mathbf{C}_{n+1}^{(i)} = diag(EA, GA, GA, GI_p, EI_{11}, EI_{22})$ is the tangent stiffness for 3D Timoshenko beam.

Similarly, $\mathbf{K}_{d,n+1}^{(i)}$ and $\mathbf{K}_{\alpha,n+1}^{(i)}$ are the consistent tangent stiffness for discontinuity.

$$\Delta \mathbf{t}_{n+1}^{(i)} = \mathbf{K}_{d,n+1}^{(i)} \Delta \mathbf{u}_{n+1}^{(i)} + \mathbf{K}_{\alpha,n+1}^{(i)} \Delta \boldsymbol{\alpha}_{n+1}^{(i)}. \tag{21}$$

Enforcing the local equation in (17), to be equal to zero, allows to use the static condensation (e.g. [3]) of the system providing elimination of the incompatible mode parameters $\boldsymbol{\alpha}$ from global equations. This leads to the reduced size of stiffness matrix, which is calculated as follows:

$$\widehat{\mathbf{K}}_{n+1}^{e,(i)} = \mathbf{K}_{n+1}^{e,(i)} - \mathbf{F}_{n+1}^{e,(i),T} (\mathbf{H}_{n+1}^{e,(i)} + K_{\alpha,n+1}^{(i)})^{-1} (\mathbf{F}_{v,n+1}^{e,(i)} + K_{d,n+1}^{(i)}). \tag{22}$$

Such a reduced stiffness matrix can be sent to the standard finite element assembly procedure to provide global set of linearized equilibrium equations. Computed incremental displacements $\Delta \mathbf{u}_{n+1}^{(i)}$ are used to perform the corresponding displacement vector update

$$\begin{aligned} &A_{e=1}^{n_{el}} \widehat{\mathbf{K}}_{n+1}^{e} \Delta \mathbf{u}_{n+1}^{(i)} = A_{e=1}^{n_{el}} \left[\mathbf{f}_{n+1}^{ext,e} - \mathbf{f}_{n+1}^{int,e,(i)} \right] \\ &\Longrightarrow \mathbf{u}_{n+1}^{(i+1)} = \mathbf{u}_{n+1}^{(i)} + \Delta \mathbf{u}_{n+1}^{(i)}. \end{aligned} \tag{23}$$

The solution of Eq. (23) requires the computation of internal force vector, $\boldsymbol{\sigma} = \begin{bmatrix} N & V & W & M_x & M_y & M_z \end{bmatrix}^T$, with the particular values of stress resultants vector. Rotations of 3D Timoshenko beams as lattice elements are kept linear elastic like in [12], while axial and two shear stress resultants undergo softening plasticity regime upon reaching failure threshold which corresponds to failure in modes I, II or III. Although the plasticity model is used in the present study, one can note that the damage model could be used as well. However, as long as we do not go to true cyclic loading applications, either of them can be successfully applied to obtain the limit load in quasi-static applications. Softening plasticity constitutive law is enforced by producing plastic deformation in the localized part of the element at the position of discontinuity. This is guided by singular part of deformation field presented with the Dirac delta function. The computation of vector $\boldsymbol{\sigma}$ can be split into scalar equations, where each translational component with potential discontinuity appears separately. In order to simplify the following presentation, we will give the evolution of softening plasticity with a scalar variable, knowing that each step is the same for all three directional components corresponding to three failure modes. Namely, the evolution equations for discontinuity can be written similarly to standard plasticity with the main difference that in softening the plastic deformation remains localized at the position of the Dirac function.

$$\begin{aligned} \dot{\alpha} &= \dot{\lambda}\frac{\partial \Phi}{\partial \sigma} = \dot{\lambda} sign(\sigma) \\ \dot{\xi} &= \dot{\lambda}\frac{\partial \Phi}{\partial q} = \dot{\lambda} \end{aligned} \tag{24}$$

where λ is the plastic multiplier associated with the softening behavior and α (also corresponding to incompatible mode parameter) is equivalent to the accumulated plastic strain at the discontinuity. The failure function involves the stress value at the point of discontinuity δ_{x_c} where the plastic strain localizes

$$\Phi(t, q) = t - (\sigma_u - q) \leq 0. \tag{25}$$

Here, t is a traction computed from (18) acting at the discontinuity, σ_u is a failure threshold and q is the internal plasticity variable for evolution of softening. When the softening constitutive law is chosen to be exponential, internal variable for plasticity can be written as

$$q = \sigma_u \left(1 - exp\left(-\xi \frac{\sigma_u}{G_f}\right)\right) \tag{26}$$

with G_f as the corresponding value of fracture energy.

In order to compute the internal variables related to discontinuity and perform the corresponding stress updates, element-wise algorithm should be performed for each directional component. Such algorithm is similar to return mapping algorithm of standard plasticity, except for the trial state computation. Computing the internal variables locally, the global solution procedure with Newton incremental/iterative procedure can be performed to give the best iterative value of displacements $u^{(i)}_{n+1}$, for which we can obtain the trial value of the traction force.

$$t^{trial}_{n+1} = -\int_0^{l_e} \overline{G}\left[EA\left(\sum_{a=1}^{2} B_a u^{(i)}_{a,n+1} + \overline{G}\alpha_n\right)\right] dx \tag{27}$$

where α_n represents the accumulated plastic deformation at the previous time step for softening plasticity. Note that we computed the trial value of traction force with regular part of strain field from (12) and that singular part (Dirac function) vanished. This holds because when keeping the stress rate bounded, one needs to ensure that the plastic multiplier λ be proportional to the Dirac function. This results with localized plastic deformation at the discontinuity and the softening law reinterpreted in distributional sense [3,5]. Computation of trial values for shear forces in the beam requires the independent internal variables α for shear directions, shear stiffness GA and strains for shear $\sum_{a=1}^{2} B_a v^{(i)}_{a,n+1} - N_a \theta^{(i)}_{a,n+1}$ and $\sum_{a=1}^{2} B_a w^{(i)}_{a,n+1} + N_a \psi^{(i)}_{a,n+1}$. The trial value of failure functions is calculated as

$$\Phi^{trial}_{n+1} = \left|t^{trial}_{n+1}\right| - (\sigma_u - q_n) \tag{28}$$

with q_n defined in (26). If the trial values of the failure functions are negative or zero, the elastic trial step is accepted for final, with no need to modify the plastic strain from the previous time step.

$$\alpha_{n+1} = \alpha_n; \quad \xi_{n+1} = \xi_n. \tag{29}$$

The plastic softening parameters remain intact, while the traction force is changed due to displacement increment. This step represents the unloading of the discontinuity which is crucial for the case when many cracks star to appear but some of them become dominant and continue to grow, while the others unload from the discontinuity. The consistent tangent stiffness for discontinuity is $\mathbf{K}^{(i)}_{d,n+1} = -\mathbf{F}^{e,(i)}_{v,n+1}$ and $\mathbf{K}^{(i)}_{\alpha,n+1} = 0$ in this case.

On the other hand, if the trial values of failure functions are positive, the current step is in the softening plasticity and internal variables should be modified to re-establish the plastic admissibility at discontinuity. The internal softening plasticity variables are updated by using evolution equations.

$$\alpha_{n+1} = \alpha_n + \lambda_{n+1} sign\left(t^{trial}_{n+1}\right) \tag{30}$$

and

$$\xi_{n+1} = \xi_n + \lambda_{n+1} \tag{31}$$

where λ_{n+1} is the softening plastic multiplier. The value of the plastic multiplier is determined from the condition $\Phi_{n+1} \leq tol$

$$\Phi_{n+1} = \Phi^{trial}_{n+1} + (q_{n+1} - q_n) + EA\overline{G}\lambda_{n+1} \leq tol. \tag{32}$$

The solution of local nonlinear equation providing the value of plastic multiplier can be obtained iteratively by using the Newton method. Finally, one can update the stress values by updated internal variables. Traction forces are produced by a change of discontinuity parameters with discontinuity tangent stiffness $\mathbf{K}^{(i)}_{\alpha,n+1} = \overline{\overline{K}}^{(i)}_{\alpha,n+1}$ and $\mathbf{K}^{(i)}_{d,n+1} = 0$. Here, $\overline{\overline{K}}^{(i)}_{\alpha,n+1}$ is obtained as the derivative of exponential softening law (26) with respect to internal variable ξ.

In order to represent the failure behavior of concrete-like materials, it is necessary to study the crack growth under mixed modes I, II and III in the presence of heterogeneities. Heterogeneous concrete samples are prepared with random process with Gaussian distribution to define the limit stress for each phase with restriction to $\pm 2\sigma$, setting mean value and standard deviation for each limit stress. The heterogeneities also play a crucial role in making the computational iterative procedure more robust by eliminating the academic case of localized failure of homogeneous material under homogeneous stress field. The computational model of this kind thus leads to more robust iterative procedure.

The three trial failure surfaces regarding three directions of local frame are defined in order to detect the softening behavior in the tension case.

$$\begin{aligned}
\Phi^{trial}_{u,n+1} &= t^{trial}_{u,n+1} - \left(\sigma_{u,t} - q_{u,n}\right) \\
\Phi^{trial}_{v,n+1} &= \left|t^{trial}_{v,n+1}\right| - \left(\tau_{u,v} - q_{v,n}\right) \\
\Phi^{trial}_{w,n+1} &= \left|t^{trial}_{w,n+1}\right| - \left(\tau_{u,w} - q_{w,n}\right)
\end{aligned} \tag{33}$$

where $\sigma_{u,t}$, $\tau_{u,v}$ and $\tau_{u,w}$ are limit stress values randomly assigned for each element using the Gaussian distribution with mean value and standard deviation. Moreover, when the softening is detected with only one of these failure surfaces, the limit stress values of other two failure surfaces are reduced to current stress computational values leading to simultaneous softening in all three failure modes.

Failure in compression case is detected by

$$\begin{aligned}
\Phi^{trial}_{u,n+1} &= \left|t^{trial}_{u,n+1}\right| - \left(\sigma_{u,c} - q_{u,n}\right) \\
\Phi^{trial}_{v,n+1} &= \left|t^{trial}_{v,n+1}\right| - \left(\tau_{f,v} - q_{v,n}\right) \\
\Phi^{trial}_{w,n+1} &= \left|t^{trial}_{w,n+1}\right| - \left(\tau_{f,w} - q_{w,n}\right)
\end{aligned} \tag{34}$$

where failure in each mode is handled independently of other two failure surfaces. Moreover, the compression force influences the failure threshold for shear sliding with the Mohr–Coulomb friction law,

$$\tau_{f,v} = \tau_{u,v} + \sigma tan(\Phi); \quad \tau_{f,w} = \tau_{u,w} + \sigma tan(\Phi) \tag{35}$$

and it magnifies the shear strength by the internal angle of friction Φ.

Table 1
Material parameters.

Cement matrix			Aggregate
$E = 15$ GPa			$E = 70$ GPa
$\nu = 0.25$			$\nu = 0.25$
Fracture limits:			
	Mean value	st. dev	–
$\sigma_{u,t}$	4 MPa	0.15	–
$\sigma_{u,c}$	40 MPa	0.5	–
$\tau_{u,v}$	1 MPa	0.1	–
$\tau_{u,w}$	1 MPa	0.1	–
Fracture energies:			
G_{fu}	6 N/m		–
G_{fv}	100 N/m		–
G_{fw}	100 N/m		–
$\Phi = 20°$			–

3. Macroscopic response: numerical homogenization

In this section we present the numerical simulations and compute the macroscopic responses for a number of different concrete specimens and various loading conditions. The computations are performed by a research version of computer program FEAP, developed by R.L. Taylor at UC Berkeley [31].

3.1. Construction of specimen

As already elaborated in the previous section, the presented approach relies on meso-scale model with cohesive links in terms of spatial beams. Such beams are generated by computing the 3D Delaunay triangulation which is performed by using Gmsh [29] over the spatial domain of interest. The edges of the resulting tetrahedral elements are converted into the beams whose cross sections are computed from the corresponding Voronoi tessellation. Such task is computed using a code written in Matlab.

3.2. Tension test

3.2.1. Uniaxial tension test

We consider here the specimen given as a cube with 15 cm side length with different volume fractions of aggregates (phase I), namely 30%, 50% and 60%. Table 1 summarizes the chosen mechanical properties for each phase. The values for shear strength (cohesion) of Portland cement are determined in agreement with empirical relations [32,33]. One can note that aggregate is much stiffer than the cement matrix and is kept linear elastic. These computations (and the subsequent ones) are all made under the displacement control with unrestrained lateral displacements for tension test.

Fig. 5 shows the macroscopic stress (sum of all reactions in the Z direction per cross-sectional area of the concrete cube) with respect to strain. The macroscopic Young modulus and limit stress which triggers the global softening change due to volume fraction of phase I for 30%, 50% and 60%. With an increase of phase I volume fraction, the global modulus of elasticity increases, as well as the elastic limit stress point. It can also be seen that when the volume fraction ratio of phase II increases, the failure of specimen becomes more ductile with larger fracture process zone (before reaching the elastic limit point) and more brittle in softening response. The main physical explanation of this influence lies in total volume of voids in concrete. The structure of cement paste is complex and there exist several sources of flaws and defects even before the application of external load, up to 50% of the volume of cement paste may consist of pores (gel pores, capillary pores and accidental or entrapped air). If we ignore all voids in aggregate (for normal aggregates these are minimal) with increasing aggregate-cement ratio, the cement paste will represent smaller proportion of specimen volume. Thus the total porosity is lower, and hence the limit stress point is higher [26].

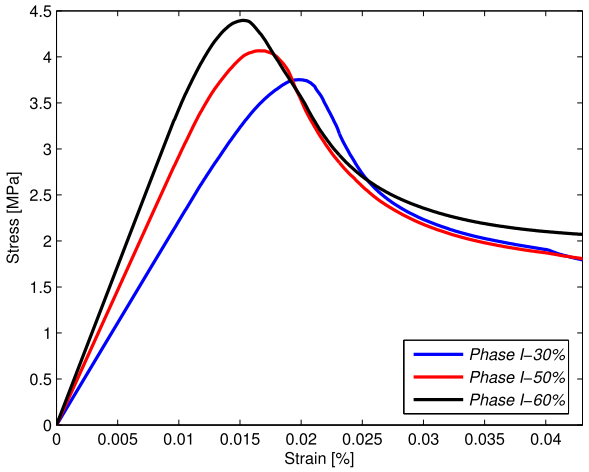

Fig. 5. Uniaxial tension test: macroscopic response for different aggregate volume fractions.

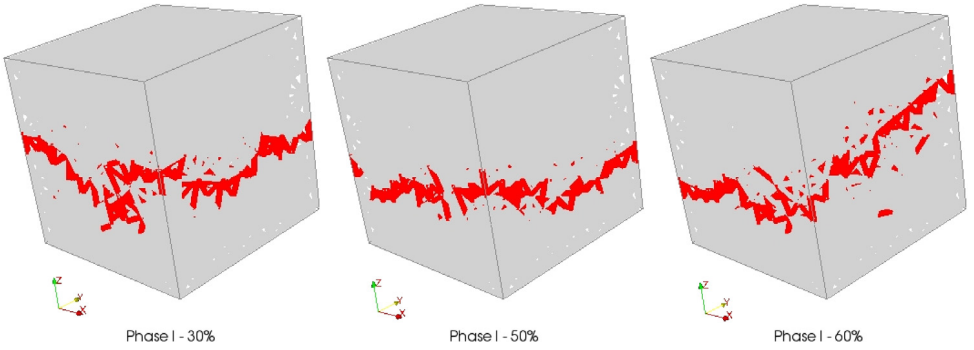

Fig. 6. Specimen contours at the end of uniaxial tension test. Beam elements in increasing softening are red colored. (For interpretation of the references to color in this figure legend, the reader is referred to the web version of this article.)

Fig. 6 presents beam elements in the subsequent stages of increasing softening at the end of tension test computation for three different heterogeneous specimens. Here, macro-crack lies in the direction perpendicular to the imposed displacement. One dominant macro-crack is present in any specimen inducing the final failure mechanism formed differently depending on the distribution of weaker phase, which decides the final crack position. Failure due to mode I is more pronounced in tension test.

Fig. 7 shows the macroscopic stress (sum of all reactions in the X, Y and Z directions per cross-sectional area of concrete cube) with respect to the strain curve for 50% volume fraction of phase I. The macroscopic limit stress which triggers the global softening changes mainly due to the beam spatial position of phase II with respect to loading direction while the macroscopic Young modulus remains unchanged. Fig. 8 presents the beam elements in increasing the softening at the end of tension test computations with 50% of phase I for each loading direction. Here again, we can note that one dominant macro-crack is present in each direction inducing the final failure mechanism.

3.2.2. Hydrostatic tension test

For simulation of hydrostatic tension test the chosen material and geometry properties remain the same as for uniaxial case (see Table 1). This computation is made under simultaneously imposed displacements along the X, Y and Z axes. Fig. 9(a) shows the macroscopic stress (sum of all reactions in the X, Y and Z directions per cross-sectional area) with respect to strain curve for 50% volume fraction of phase I. In Fig. 9(b), the comparison in the X direction between macroscopic stresses for 50% volume fraction of phase I obtained in uniaxial tension test and in hydrostatic case is given. It can be noted that the hydrostatic response is stiffer and less ductile comparing to the uniaxial response.

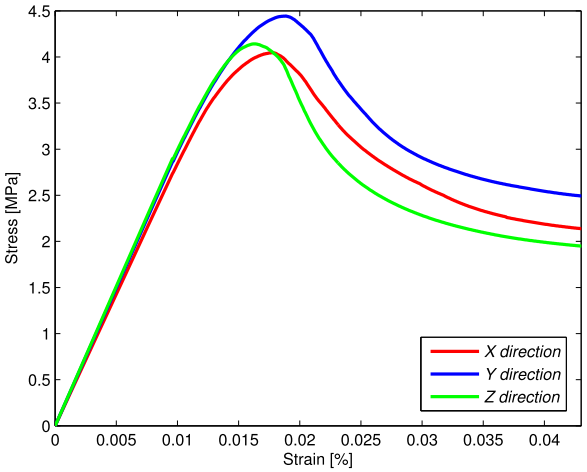

Fig. 7. Uniaxial tension test: macroscopic responses for specimen (phase I-50%) in three loading directions.

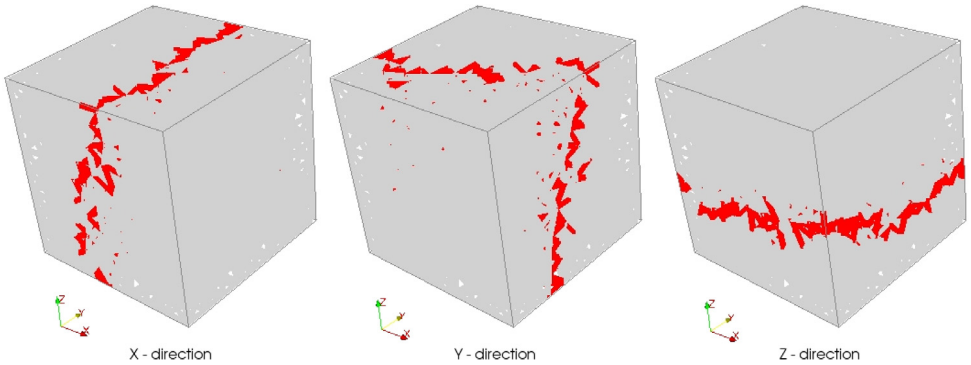

Fig. 8. Specimen contours at the end of uniaxial tension test for phase I-50% specimen in all three loading directions. Beam elements in increasing softening are red colored. (For interpretation of the references to color in this figure legend, the reader is referred to the web version of this article.)

Fig. 10 presents the beam elements in increasing softening at the end of hydrostatic tension test computations. We can observe several macro-cracks contrary to a simple tension test where only one macro-crack is observed.

3.3. Compression test

The results of numerical simulations and corresponding macroscopic responses for specimens under uniaxial (unconfined) compression loading program are given here. Simulations in compression test are conducted with displacement control, while lateral displacements are restrained which corresponds to the case with higher friction between the load platen and the specimen. Geometric, material parameters and the distribution of aggregate and cement paste are the same as for the previously used specimens (see Table 1). Macroscopic responses (Fig. 11(a)) reveal the change in modulus of elasticity and elastic limit stress point due to different volume fractions of aggregate. With an increase of phase I, the global modulus of elasticity and elastic limit point increase similar to tension test case. The difference with respect to uniaxial tension test mechanism concerns the ductile phase of the response during creation of the fracture process zone, which is more pronounced in compression test than in tension test. Thus, not only the ductile part with fracture process zone is larger, but also its contribution to total dissipation compression failure. The main reason for this is that more elements are subjected to shear and compression simultaneously, where crack propagates because of the shear, which leads to mode II or mode III failure. If the crack propagates in mode II or III, it is still possible to transfer the compression force through the specimen, assuming that two separated blocks

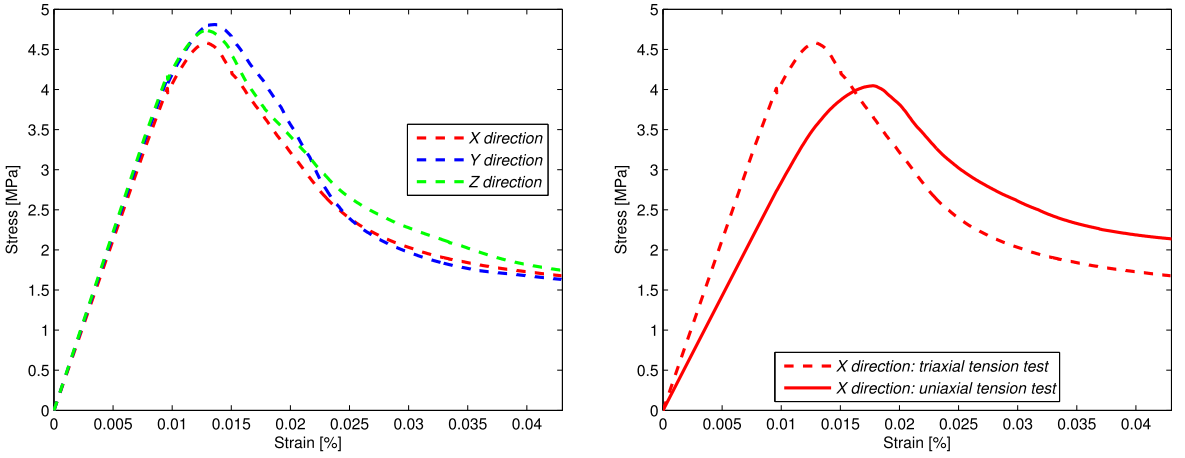

Fig. 9. Macroscopic response—phase I-50%: (a) hydrostatic tension test; (b) hydrostatic-uniaxial tension test comparison for the X direction.

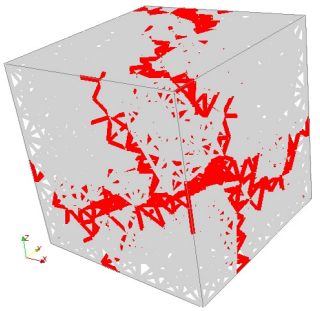

Fig. 10. Specimen contour at the end of hydrostatic tension test for phase I-50% specimen. Beam elements in increasing softening are red colored. (For interpretation of the references to color in this figure legend, the reader is referred to the web version of this article.)

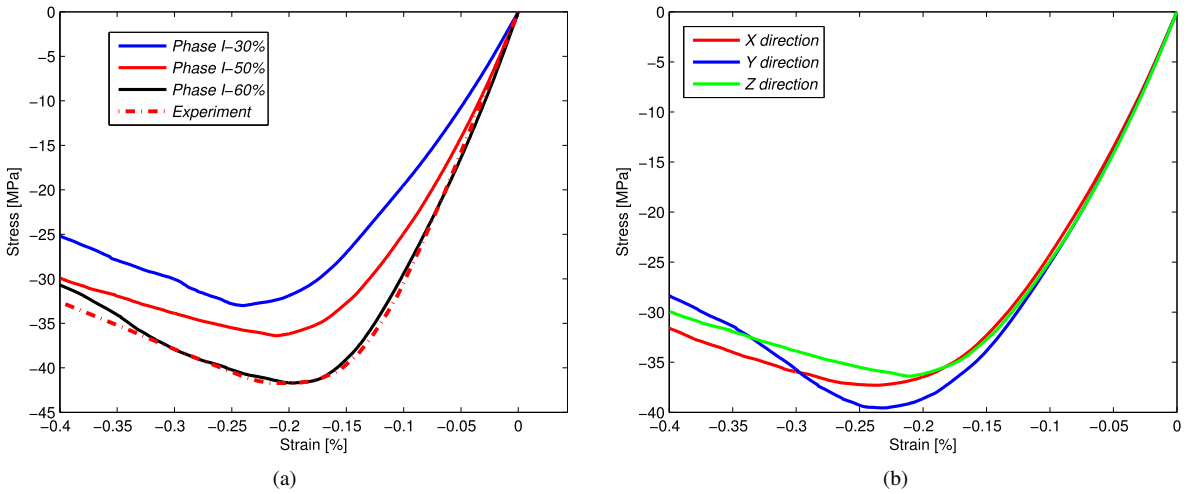

Fig. 11. Macroscopic response for uniaxial compression test: (a) different aggregate volume fractions; (b) phase I-50%.

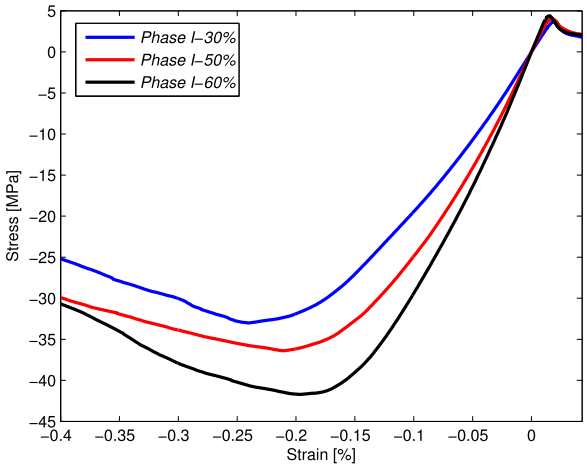

Fig. 12. Complete macroscopic response for different aggregate volume fractions.

formed during cracking in mode II or III, lean on each other. Compression force in this situation increases until the point where significant damage on the specimen is made, and until cracking is extensive enough that loading capacity starts to decrease. One can note that the macroscopic response for numerical specimen with 60% of aggregate fits very well with the experimental results conducted on the concrete cube with similar properties taken from [34].

Fig. 11(b) shows the macroscopic stress (sum of all reactions in the X, Y and Z directions per cross-sectional area) versus strain curve for 50% volume fraction of phase I. The macroscopic limit stress which triggers the softening changes mainly due to the beam spatial position of phase II with respect to loading direction while the macroscopic Young modulus remains unchanged as in the tension case.

In order to compare the macroscopic responses corresponding to uniaxial tension and compression, Fig. 12 presents the macroscopic curves and reveals that the overall compression–tension ratio is equal to 8.8, 9.37 and 9.50 for, respectively, 30%, 50% and 60% of phase I.

Fig. 13 (upper row) presents beam elements in increasing softening at the end of compression test computations for phase I-50% specimen in three loading directions. Contrary to tension test crack patterns, in compression test much more macro-cracks are needed to drive the specimens to failure and these are influenced more by mode II and mode III mechanisms, which form the final crack patterns together with mode I. Fig. 13 (lower row) reveals the displacements in beam elements at the end of compression test computations which correspond to the upper row figures. Here, we can see clearly that the diagonal orientation failure mode is dominant.

3.4. Failure surfaces for biaxial loading

In this section we show how to obtain the macroscopic multi-surface criterion for concrete-like materials by taking into account heterogeneities and different processes of cracking using the meso-scale model proposed in the previous section. The most appropriate combination of multi-surface models for concrete can be considered by combining Drucker–Prager for compression stress and Rankine for tensile stress with the plasticity model describing the failure of structure. It can be written in terms of the principal stress values according to

$$\begin{aligned} \Phi^{DP} &= \sqrt{J_2} + \mu I_1/\sqrt{6} - (f_c - \hat{q}^c(\xi^c)) \leq 0 \\ \Phi_i^R &= \sigma_i - (f_t - \hat{q}^t(\xi^t)) \leq 0 \end{aligned} \tag{36}$$

where Φ^{DP} and Φ_i^R are, respectively, the Drucker–Prager and Rankine yield surfaces, σ_i, J_2 and I_1 are the principal values, the second and the first invariant of stress tensor, f_c and f_t are compressive and tensile yield stress values, q^c and q^t are the corresponding internal variables that control the plasticity threshold evolution resulting with desired amount of fracture energy for any particular mode of localized failure [24].

In addition to this criterion we can find the coupled plasticity-damage model [35] and the Saint-Venant multisurface criterion [36]. The coupled plasticity-damage model components are selected in order to provide the representation of

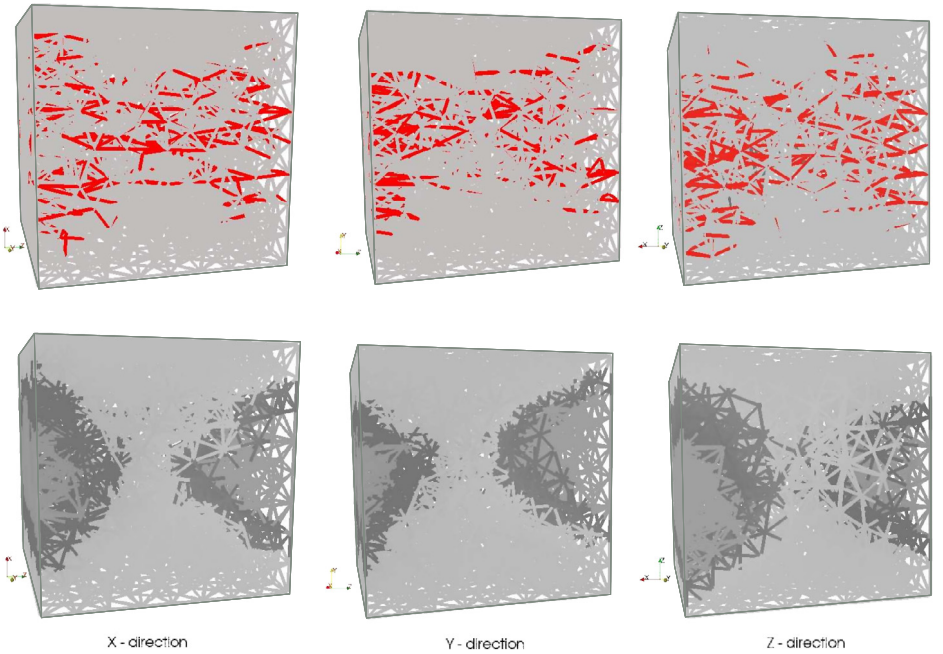

Fig. 13. Specimen contour at the end of uniaxial compression test for phase I-50% specimen in three loading directions. Beam elements in increasing softening are red colored (upper row), displacements in the direction perpendicular to loading direction (lower row). (For interpretation of the references to color in this figure legend, the reader is referred to the web version of this article.)

concrete in compaction where the plastic component is given in terms of the Drucker–Prager criterion and the damage criterion in terms of the spherical part of the stress tensor:

$$\begin{aligned} \Phi^p(\boldsymbol{\sigma}) &= \sqrt{J_2} + tan(\alpha)\frac{1}{3}tr(\boldsymbol{\sigma}) - \sqrt{2/3}\sigma_f^p \\ \Phi^d(\boldsymbol{\sigma}, q^d) &= tr(\boldsymbol{\sigma}) - (\sigma_f^d - q^d) \end{aligned} \tag{37}$$

where $tan(\alpha)$ is the material parameter which can characterize the internal friction, σ_f^d is the elasticity limit point for damage and q^d is the hardening damage variable.

Furthermore, we can express the Saint-Venant multisurface plasticity criterion directly in the stress space, in terms of principal values of stress tensor:

$$\begin{aligned} \Phi_1(\boldsymbol{\sigma}) &= \frac{\bar{\lambda} + 2\mu}{2\mu}\sigma_1 - \frac{\bar{\lambda}}{2\mu}\sigma_2 - \sigma_y \leq 0 \\ \Phi_2(\boldsymbol{\sigma}) &= -\frac{\bar{\lambda}}{2\mu}\sigma_1 + \frac{\bar{\lambda} + 2\mu}{2\mu}\sigma_2 - \sigma_y \leq 0 \end{aligned} \tag{38}$$

where the value of elasticity limit point is obtained from the biaxial tension test.

In order to test the biaxial failure behavior, we choose the plate specimen with the dimensions of 150 mm × 30 m × 150 mm. The plate is subjected to biaxial imposed displacements, producing the following stress combinations: tension–tension, compression–compression, compression–tension and tension–compression (Fig. 14). Uniaxial compressive strength value is taken from the uniaxial compressive test performed on plate concrete specimen for 6 different distributions of each phase with 50% of aggregates volume (Table A.3).

Fig. 15 shows the macroscopic tension and compression stress (sum of all reactions in the X direction per cross-sectional area) versus strain curve for 6 realizations with 50% volume fraction of phase I. Macroscopic responses reveal the changes in the elastic limit point mainly due to the different spatial beam positions of phase II with respect to loading direction.

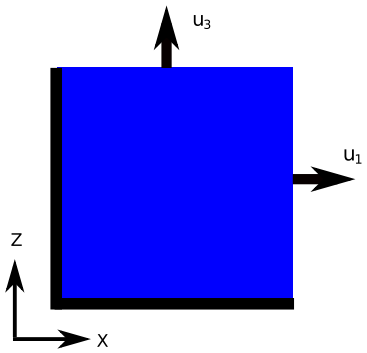

Fig. 14. Specimen for biaxial test: boundary conditions and loading.

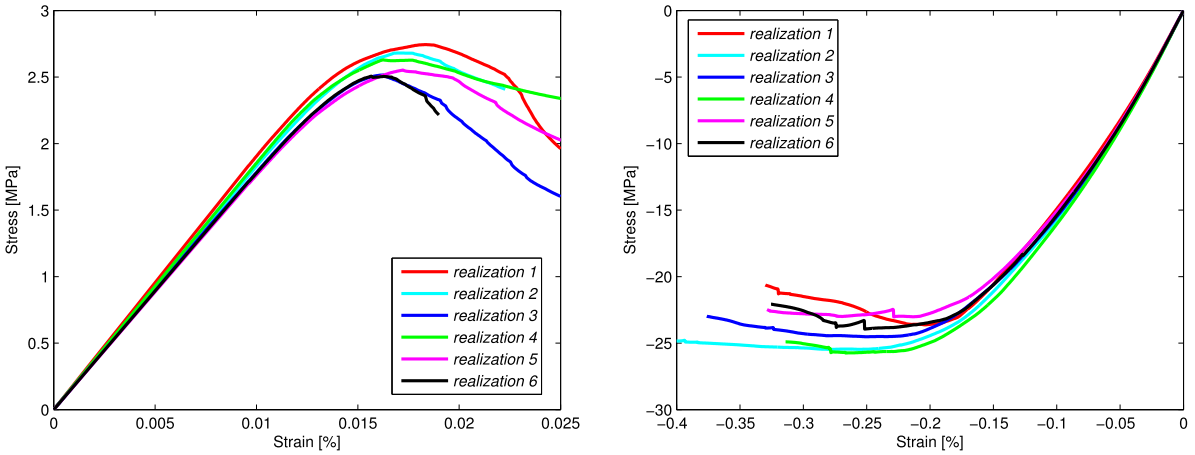

Fig. 15. Uniaxial macroscopic response for 6 realizations in plate specimen: (a) tension test; (b) compression test.

In order to obtain four loading combinations (compression–compression, tension–tension, compression–tension and tension–compression), we perform a circular loading program based upon the trigonometrical circle $cos(\alpha)^2 + sin(\alpha)^2 = 1$. Thus, couples of imposed displacements ($u_1 = cos(\alpha)$, $u_3 = sin(\alpha)$) are parametrized in terms of angle α. Faces X = 150 mm and Z = 150 mm are, respectively, subjected to imposed displacements u_1 and u_3, while faces X = 0 mm and Z = 0 mm are blocked in the X and Z directions (Fig. 14). Compressive and tensile are chosen with negative and positive values, respectively. Stress in the principal direction 1 (X direction) is labeled as $\overline{\sigma}_1$ and stress in the principal direction 3 (Z direction) as $\overline{\sigma}_3$. The ultimate strength in the principal direction 1 is written σ_1 and the one in the direction 3, σ_3. Tables A.4 and A.5 (see Appendix) contain all the computed data on the ratio of ultimate strengths σ_1 and σ_3 with respect to σ_{ci} under different values of imposed displacements.

Graphical representations of Tables A.4 and A.5 are presented in Fig. 16(a) (1 realization) and (b) (6 realizations), while Fig. 17 shows the evolution of σ_1/σ_{ci} with respect to σ_3/σ_{ci} during loading until failure for realization 1. Fig. 16(b) also provides some plots of failure criteria: the Drucker–Prager and the Rankine from Eq. (36), coupled plasticity-damage from Eq. (37) and the Saint-Venant multisurface from Eq. (38). The results computed with the proposed model best fits with the multisurface Drucker–Prager Rankine criterion and experimental results on biaxial specimens taken from [34]. Table 2 contains the computed macroscopic fracture energies under particular couples of imposed displacements for realization 1 (red dots). Macroscopic differences between uniaxial and biaxial tests on a plate specimen for tension case can be observed (Fig. 18). It can be noted that in biaxial response strength increase is observed compared to the uniaxial one. Moreover, specimen is also less ductile in biaxial loading condition than

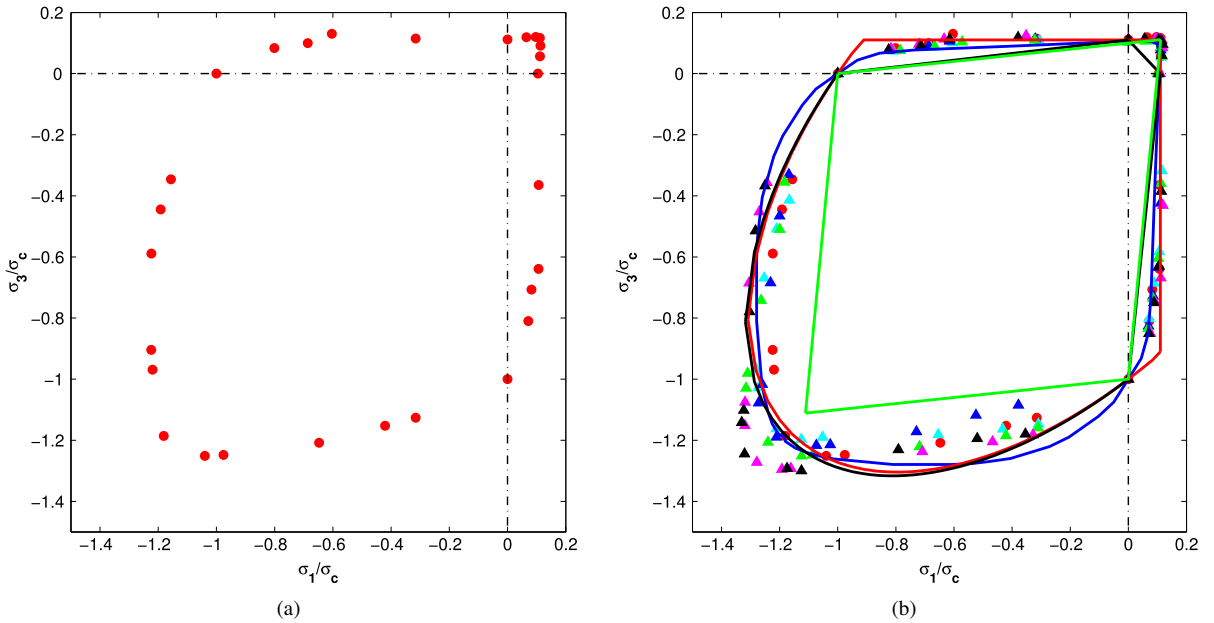

Fig. 16. Failure surfaces: (a) for realization 1; (b) for 6 realizations with the multisurface Drucker–Prager–Rankine surface (red line—Eq. (36)), coupled plasticity-damage model (black line—Eq. (37)), Saint-Venant (green line—Eq. (38)) and experimental (blue line). (For interpretation of the references to color in this figure legend, the reader is referred to the web version of this article.)

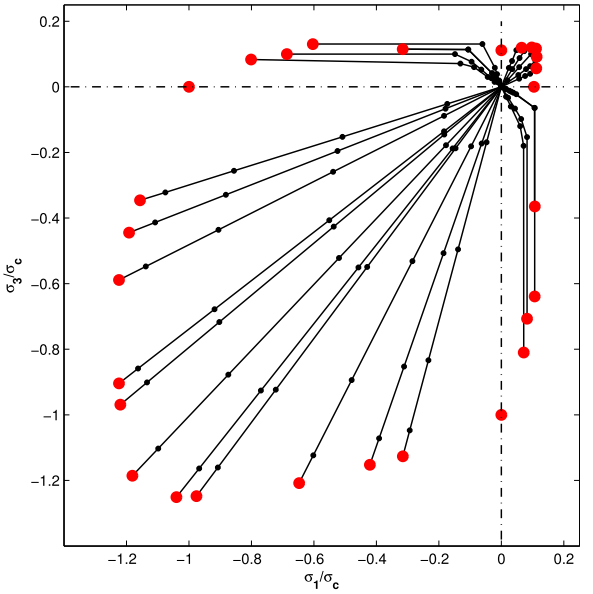

Fig. 17. Evolution of σ_1/σ_{ci} with respect to σ_3/σ_{ci} during loading until failure for realization 1 (red dots). (For interpretation of the references to color in this figure legend, the reader is referred to the web version of this article.)

in uniaxial response either. The same is observed for biaxial compression case. The contours of the plate specimens can be observed in Fig. 19 with red colored beam elements in increasing softening regime at the end of both tension (upper row) and compression test (lower row) computations.

Symmetrical failure behavior of concrete in relation with the 45° line under biaxial loading is observed in Fig. 16(a) and (b) as well as in the experimental approaches [37]. As already shown, the ultimate compression strength of concrete is higher under biaxial compression test than in uniaxial compression. Most likely, this happens due to

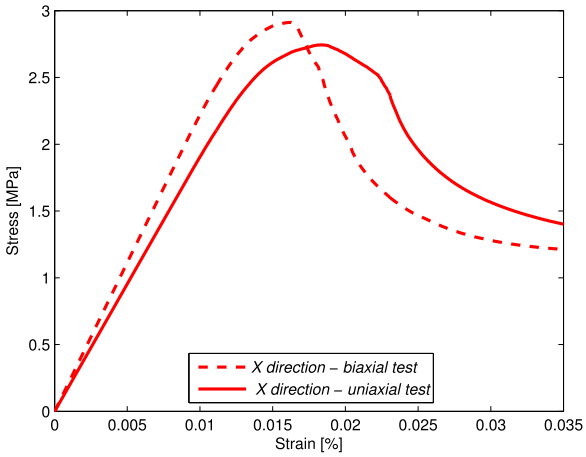

Fig. 18. Biaxial–uniaxial test comparison for realization 1—phase I-50%: macroscopic response in the X direction—tension test.

Table 2
Fracture energy under particular couples of imposed displacements for realization 1 (red points).

Combined regions	u_1 (mm), u_3 (mm)	G_f (N/m)
Tension–tension	0.0200,0.0200	6.525
Compression–compression	−0.2000,−0.2000	357.351
Tension–compression	0.0224,−0.0380	73.157
Compression–tension	−0.0380,0.0224	72.241

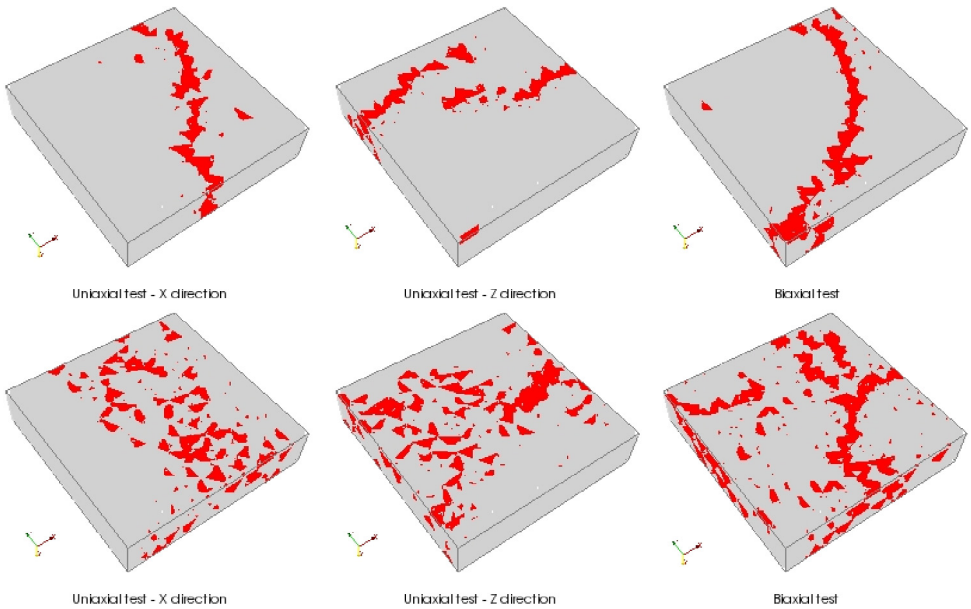

Fig. 19. Plate specimen contours at the end of uniaxial and biaxial tension test (upper row) and compression test (lower row). Beam elements in increasing softening are red colored. (For interpretation of the references to color in this figure legend, the reader is referred to the web version of this article.)

concrete compaction effect leading to decrease in porosity during biaxial compression test. Increase of ultimate biaxial compression strength in relation to the corresponding uniaxial compression strength is observed for each couples of imposed displacement in the compression–compression region. Maximum value of ultimate compression strength is obtained for imposed displacements $u_1 = -0.1800$ mm, $u_3 = -0.0872$ mm and $u_1 = -0.0872$ mm,

$u_3 = -0.1800$ mm for σ_1 and σ_3, respectively, in each realization. In the tension–tension region the value of the concrete ultimate strength for each couples of imposed displacement is very close to the corresponding uniaxial tensile strength. Finally, in the tension–compression and compression–tension regions, the concrete compression ultimate strength increases while the tension decreases.

Fig. 17 shows that in the region compression–compression, the behavior of concrete is linear between σ_1/σ_{ci} and σ_3/σ_{ci} due to prevented cracks opening. Moreover, biaxial compression loading in the X and Z directions tends to prevent crack opening, respectively, in the Z and X directions and dominant failure mechanism occurs in the Y direction (out of plane). For other regions (tension–tension, tension–compression, compression–tension), the linear relation between σ_1/σ_{ci} and σ_3/σ_{ci} is first observed until cracking is not present, and non-linear relation between these two ratios, where cracking is more pronounced. In regions tension–compression and compression–tension one can note that the ultimate tension strength is sooner reached rather than for compression due to the higher ratio of imposed displacements.

4. Conclusions

In this work we proposed the meso-scale constitutive model for concrete employing a three-dimensional beam lattice model. We confirmed the model capability to represent the salient features of failure phenomena for concrete-like materials. The model is able to provide the corresponding variability of material parameters for macro-scale failure criterion, combining the Drucker–Prager for compression stress and the Rankine for tensile stress. The numerical tests carried out with a meso-scale model consider different volume fractions of cohesive links or spatial beam elements representing cement paste and aggregates in agreement with the chosen granulometric curve. The beam element is represented by 3D Timoshenko beam, embedded with strong discontinuities in the local coordinate system directions, which provide the capability to simulate the localized failure in modes I, II and III. Failure can occur individually in any mode or in mixed mode. The failure criteria is different under tension or compression force. In the tension case, softening is activated simultaneously for all modes as soon as one failure surface becomes active, whereas in compression the failure modes are handled separately. The compression force influences the shear strength threshold in the Mohr–Coulomb manner. Another feature of the model is that each material phase parameters are introduced through the Gaussian distribution representing heterogeneities of each phase. We illustrated here that the model of this kind can be used successfully to present quite complex macroscopic responses. Three concrete specimens with 30%, 50% and 60% volume fractions of aggregate were subjected to uniaxial tension and compression tests. We confirm that the resistance to tension is much lower than the one in compression. We can observe one dominant macro-crack that leads to specimen failure in tension case, whereas for compression case many more macro-cracks are needed to drive the specimens to failure, with a significant contribution of mode II and mode III mechanisms. We also find that ultimate strength increases with the increase of volume fraction of aggregates, and also influences the crack path. Overall compression–tension ratio σ_c/σ_t is equal to 8.8, 9.37 and 9.50 for 30%, 50% and 60% of phase I, respectively. All these points fit well with the typical observations made for concrete-like materials [38,39].

Finally, one of the most significant findings is that this approach can provide the definition of the parameters, such as the fracture energy, ultimate strength taking into account the heterogeneity and different processes of cracking governing the final failure mechanism. This approach can also be used for parameters identification of multi-surface models (e.g. coupled plasticity-damage model [35], Saint-Venant plasticity model [36] or combination of the Rankine and the Drucker–Prager criteria [40]) providing more predictive results from classical phenomenological models in the structural analysis. Such task is carried in Part II of this paper.

The proposed meso-scale model provides many enhanced features, but also requires a more refined procedure to obtain the model parameters, and their distribution typical of material heterogeneities. The subsequent work, presented in Part II of this paper, describes the solution to inverse identification problem by using coupled nonlinear mechanics–probability approach to provide not only the parameters, but also their probability distribution. This pertains not only to elastic model parameters, but also to all different parameters governing the complete failure process. The latter requires very careful description of the experimental procedure and the ability to provide the corresponding computational result to any given measurement, as well as the most extensive set of experimental results.

Acknowledgments

This work was supported jointly by Haut-de-France Region (CR Picardie) (120-2015-RDISTRUCT-000010 and RDISTRUCT-000010) and EU funding (FEDER) for Chaire-de-Mecanique (120-2015-RDISTRUCTF-000010 and RDISTRUCTI-000004) and a scholarship by French Embassy in Sarajevo. This support is gratefully acknowledged.

Table A.3
Uniaxial strength with 50% of aggregates.

Realization j	Direction i	Tension strength σ_{ti}^{j} (MPa)	Compressive strength σ_{ci}^{j} (MPa)
1	1(X)	2.744	−24.767
	3(Z)	2.636	−23.266
2	1(X)	2.681	−25.477
	3(Z)	2.696	−26.197
3	1(X)	2.515	−24.520
	3(Z)	2.703	−25.456
4	1(X)	2.588	−25.739
	3(Z)	2.742	−26.580
5	1(X)	2.509	−23.033
	3(Z)	2.554	−23.017
6	1(X)	2.507	−23.946
	3(Z)	2.641	−23.560

Table A.4
Ratios of ultimate strength with respect to σ_c along the X and Z directions under different couples of imposed displacements for realization 1, 2 and 3.

Combined regions	u_1 (mm), u_3 (mm)	σ_1^1/σ_c^1	σ_3^1/σ_c^1	σ_1^2/σ_c^2	σ_3^2/σ_c^2	σ_1^3/σ_c^3	σ_3^3/σ_c^3
Tension–tension	0.0000,0.0200	0.000	0.112	0.000	0.103	0.000	0.106
	0.0173,0.0100	0.113	0.091	0.113	0.083	0.112	0.086
	0.0100,0.0173	0.097	0.120	0.100	0.108	0.099	0.113
	0.0200,0.0000	0.104	0.000	0.105	0.000	0.103	0.000
	0.0056,0.0192	0.065	0.119	0.057	0.108	0.057	0.113
	0.0192,0.0056	0.112	0.057	0.113	0.054	0.111	0.078
	0.0200,0.0200	0.111	0.117	0.109	0.105	0.110	0.108
Compression–compression	0.0000,−0.2000	0.000	−1.000	0.000	−1.000	0.000	−1.000
	−0.1732,−0.1000	−1.220	−0.969	−1.273	−1.028	−1.272	−1.077
	−0.1000,−0.1732	−1.040	−1.251	−1.126	−1.197	−1.074	−1.216
	−0.2000,0.0000	−1.000	0.000	−1.000	0.000	−1.000	0.000
	−0.0872,−0.1800	−0.976	−1.248	−1.052	−1.190	−1.026	−1.214
	−0.1800,−0.0872	−1.224	−0.862	−1.280	−0.966	−1.260	−1.017
	−0.2000,−0.2000	−1.181	−1.186	−1.211	−1.162	−1.211	−1.190
	−0.1990,−0.0200	−1.192	−0.445	−1.210	−0.508	−1.200	−0.466
	−0.0200,−0.1990	−0.421	−1.152	−0.432	−1.163	−0.524	−1.118
	−0.1950,−0.0444	−1.224	−0.589	−1.253	−0.669	−1.231	−0.685
	−0.0444,−0.1950	−0.647	−1.208	−0.654	−1.181	−0.729	−1.172
	−0.2000,−0.0020	−1.156	−0.346	−1.167	−0.414	−1.168	−0.330
	−0.0020,−0.2000	−0.315	−1.126	−0.309	−1.147	−0.378	−1.085
Tension–compression	0.1732,−0.1000	0.107	−0.639	0.106	−0.583	0.103	−0.634
	0.1936,−0.0500	0.106	−0.512	0.115	−0.318	0.111	−0.424
	0.0224,−0.0380	0.071	−0.810	0.071	−0.802	0.069	−0.826
	0.0173,−0.0200	0.082	−0.707	0.089	−0.686	0.085	−0.728
Compression–tension	0.1732,−0.1000	−0.604	0.130	−0.606	0.101	−0.615	0.106
	0.1936,−0.0100	−0.507	0.124	−0.306	0.107	−0.321	0.114
	0.0224,−0.0380	−0.801	0.083	−0.809	0.074	−0.817	0.076
	0.0173,−0.0200	−0.686	0.100	−0.680	0.087	−0.686	0.090

Table A.5
Ratios of ultimate strength with respect to σ_c along the X and Z directions under different couples of imposed displacements for realization 4, 5 and 6.

Combined regions	u_1 (mm),u_3 (mm)	σ_1^4/σ_c^4	σ_3^4/σ_c^4	σ_1^5/σ_c^5	σ_3^5/σ_c^5	σ_1^6/σ_c^6	σ_3^6/σ_c^6
Tension–tension	0.0000,0.0200	0.000	0.103	0.000	0.111	0.000	0.112
	0.0173,0.0100	0.113	0.087	0.119	0.095	0.117	0.096
	0.0100,0.0173	0.097	0.107	0.100	0.114	0.104	0.110
	0.0200,0.0000	0.101	0.000	0.109	0.000	0.105	0.000
	0.0056,0.0192	0.058	0.107	0.094	0.114	0.056	0.113
	0.0192,0.0056	0.114	0.056	0.117	0.086	0.115	0.059
	0.0200,0.0200	0.107	0.106	0.115	0.111	0.114	0.108
Compression–compression	0.0000,−0.2000	0.000	−1.000	0.000	−1.000	0.000	−1.000
	−0.1732,−0.1000	−1.316	−1.030	−1.319	−1.152	−1.330	−1.142
	−0.1000,−0.1732	−1.124	−1.251	−1.192	−1.295	−1.175	−1.292
	−0.2000,0.0000	−1.000	0.000	−1.000	0.000	−1.000	0.000
	−0.0872,−0.1800	−1.087	−1.248	−1.161	−1.292	−1.125	−1.300
	−0.1800,−0.0872	−1.310	−0.981	−1.319	−1.075	−1.324	−1.101
	−0.2000,−0.2000	−1.240	−1.206	−1.279	−1.272	−1.320	−1.244
	−0.1990,−0.0200	−1.200	−0.510	−1.270	−0.452	−1.283	−0.514
	−0.0200,−0.1990	−0.421	−1.185	−0.467	−1.205	−0.520	−1.194
	−0.1950,−0.0444	−1.264	−0.742	−1.305	−0.685	−1.304	−0.779
	−0.0444,−0.1950	−0.719	−1.221	−0.709	−1.237	−0.791	−1.231
	−0.2000,−0.0020	−1.183	−0.355	−1.244	−0.357	−1.250	−0.367
	−0.0020,−0.2000	−0.311	−1.159	−0.328	−1.182	−0.354	−1.180
Tension–compression	0.1732,−0.1000	0.103	−0.604	0.111	−0.669	0.105	−0.630
	0.1936,−0.0500	0.112	−0.359	0.119	−0.431	0.113	−0.385
	0.0224,−0.0380	0.069	−0.834	0.076	−0.850	0.071	−0.850
	0.0173,−0.0200	0.084	−0.735	0.093	−0.749	0.088	−0.749
Compression–tension	0.1732,−0.1000	−0.572	0.104	−0.634	0.113	−0.615	0.113
	0.1936,−0.0100	−0.322	0.110	−0.352	0.125	−0.379	0.119
	0.0224,−0.0380	−0.785	0.075	−0.817	0.082	−0.825	0.078
	0.0173,−0.0200	−0.666	0.088	−0.721	0.096	−0.714	0.092

Appendix. Tables

See Tables A.3–A.5.

References

[1] N.N. Bui, M. Ngo, M. Nikolic, D. Brancherie, A. Ibrahimbegovic, Enriched timoshenko beam finite element for modeling bending and shear failure of reinforced concrete frames, Comput. & Structures 143 (2014) 9–18.

[2] M. Nikolic, E. Karavelic, A. Ibrahimbegovic, P. Miscevic, Lattice element models and their peculiarities, Arch. Comput. Methods Eng. (2017). http://dx.doi.org/10.1007/s11831-017-9210-y.

[3] A. Ibrahimbegovic, Nonlinear Solid Mechanics: Theoretical Formulations and Finite Element Solution Methods, Springer, London, 2009.

[4] J.G. Rots, S. Invernizzi, Regularized sequentially linear saw-tooth softening model, Int. J. Numer. Anal. Methods Geomech. 28 (2004) 821–856.

[5] J.C. Simo, J. Oliver, F. Armero, An analysis of strong discontinuities induced by strain-softening in rate-independent inelastic solids, Comput. Mech. 12 (1993) 277–296.

[6] M. Ortiz, Y. Leroy, A. Needleman, A finite element method for localization failure analysis, Comput. Methods Appl. Mech. Engrg. 61 (1987) 189–214.

[7] A. Ibrahimbegovic, D. Brancherie, Combined hardening and softening constitutive model of plasticity: precursor to shear slip line failure, Comput. Mech. 31 (2003) 88–100.

[8] A. Ibrahimbegovic, S. Melnyk, Embedded discontinuity finite element method for modeling of localized failure in heterogeneous materials with structured mesh: an alternative to extended finite element method, Comput. Mech. 40 (2007) 149–155.

[9] A. Ibrahimbegovic, E. Wilson, A modified method of incompatible modes, Commun. Appl. Numer. Methods 7 (1991) 187–194.

[10] M. Nikolic, A. Ibrahimbegovic, P. Miscevic, Brittle and ductile failure of rocks: Embedded discontinuity approach for representing mode I and mode II failure mechanisms, Internat. J. Numer. Methods Engrg. 102 (2015) 1507–1526.

[11] M. Nikolic, A. Ibrahimbegovic, P. Miscevic, Discrete element model for the analysis of fluid-saturated fractured poro-plastic medium based on sharp crack representation with embedded strong discontinuities, Comput. Methods Appl. Mech. Engrg. 298 (2016) 407–427.

[12] M. Nikolic, A. Ibrahimbegovic, Rock mechanics model capable of representing initial heterogeneities and full set of 3D failure mechanisms, Comput. Methods Appl. Mech. Engrg. 290 (2015) 209–227.
[13] G. Cusatis, D. Pelessone, A. Mencarelli, Lattice discrete particle model (LDPM) for failure behavior of concrete. I: theory, Cem. Concr. Compos. 33 (2011) 881–890.
[14] E. Schlangen, E.J. Garboczi, New method for simulating fracture using an elastically uniform random geometry lattice, Internat. J. Engrg. Sci. 34 (1996) 1131–1144.
[15] E. Schlangen, J.G.M. VanMier, Simple lattice model for numerical simulation of fracture of concrete materials and structures, Mater. Struct. 25 (1992) 534–542.
[16] E. Schlangen, J.G.M. Van Mier, Experimental and numerical analysis of micromechanisms of fracture of cement-based composites, Cem. Concr. Compos. 14 (1992) 105–118.
[17] G. Cusatis, Z. Bazant, L. Cedolin, Confinement-shear lattice CSL model for fracture propagation in concrete, Comput. Methods Appl. Mech. Engrg. 195 (2006) 7154–7171.
[18] G. Lilliu, J.G.M. van Mier, 3D lattice type fracture model for concrete, Eng. Fract. Mech. 70 (2003) 927–941.
[19] S. Berton, J.E. Bolander, Crack band model of fracture in irregular lattices, Comput. Methods Appl. Mech. Engrg. 195 (2006) 7172–7181.
[20] P. Grassl, M. Jirasek, Meso-scale approach to modelling the fracture process zone of concrete subjected to uniaxial tension, Int. J. Solids Struct. 47 (2010) 957–968.
[21] P. Grassl, D. Gregoire, L.R. Solano, G. Pijaudier-Cabot, Meso-scale modelling of the size effect on the fracture process zone of concrete, Int. J. Solids Struct. 49 (2012) 1818–1827.
[22] M. Vassaux, C. Oliver-Leblond, B. Richard, F. Ragueneau, Beam-particle approach to model cracking and energy dissipation in concrete: Identification strategy and validation, Cem. Concr. Compos. 70 (2016) 1–14.
[23] N. Benkemoun, M. Hautefeuille, J.B. Colliat, A. Ibrahimbegovic, Failure of heterogeneous materials: 3D meso-scale FE models with embedded discontinuities, Internat. J. Numer. Methods Engrg. 82 (2010) 1671–1688.
[24] N. Benkemoun, A. Ibrahimbegovic, J.B. Colliat, Anisotropic constitutive model of plasticity capable of accounting for details of meso-structure of two-phase composite material, Comput. & Structures 90–91 (2012) 153–162.
[25] E. Schlangen, E.J. Garboczi, Fracture simulations of concrete using lattice models: computational aspects, Eng. Fract. Mech. 57 (1997) 319–332.
[26] A.M. Neville, J.J. Brooks, Concrete Technology, second ed., Prentice Hall, 2010.
[27] J. Lubliner, Plasticity Theory, Mac-Millan, 1990.
[28] J. Lemaitre, J.-L. Chaboche, Mecanique Des Materiaux Solides, Dunod, 2004.
[29] C. Geuzaine, J.F. Remacle, Gmsh: a three-dimensional finite element mesh generator with built-in pre- and post-processing facilities, Internat. J. Numer. Methods Engrg. 11 (2009) 1309–1331.
[30] A. Ibrahimbegovic, A. Delaplace, Microscale and mesoscale discrete models for dynamic fracture of structures built of brittle materials, Comput. Struct. 81 (2003) 1255–1265.
[31] R.L. Taylor, FEAP Finite element Analysis Program. University of California, Berkeley, http://www.ce.berkeley.edu.rlt.
[32] M. Moosavi, W.F. Bawden, Shear strength of Portland cement grout, Cem. Concr. Compos. 25 (2003) 729–735.
[33] I. Yoshitake, T. Uno, A. Scanlon, Simplified test of cracking strength of concrete element subjected to pure shear, J. Mater. Civ. Eng. 23 (2011) 999–1006.
[34] S. Mindess, J.F. Young, D. Darwin, Concrete, second ed., Prentice Hall, 2003.
[35] A. Ibrahimbegovic, D. Markovic, F. Gatuingt, Constitutive model of coupled damage-plasticity and its finite element implementation, Rev. Eur. Des. Elem. Finis 12 (2003) 381–405.
[36] J.B. Colliat, A. Ibrahimbegovic, L. Davenne, SaintVenant multisurface plasticity model in strain space and in stress resultants, Eng. Comput. 22 (2005) 536–557.
[37] L. Sang-Keun, S. Young-Chul, H. Sang-Hoon, Biaxial behavior of plain concrete of nuclear containment building, Nucl. Eng. Des. 227 (2004) 143–153.
[38] H. Kupfer, H.K. Hilsdorf, Behavior of concrete under biaxial stress, ACI J. Proc. 66 (1969) 656–666.
[39] A. Carpinteri, A.R. Ingraffea, Fracture mechanics of concrete, Martinus Nijhoff editor, The Netherlands, 1984.
[40] S. Dolarevic, A. Ibrahimbegovic, A modified three-surface elasto-plastic cap model and its numerical implementation, Comput. Struct. 85 (2007) 419–430.